Achieving Centimeter-Accuracy Indoor Localization on WiFi Platforms: A Multi-Antenna Approach

Chen Chen, *Student Member, IEEE*, Yan Chen, *Senior Member, IEEE*, Yi Han, *Student Member, IEEE*, Hung-Quoc Lai, Feng Zhang, *Student Member, IEEE*, and K. J. Ray Liu, *Fellow, IEEE*

***Abstract*—Channel frequency response (CFR) is a fine-grained location-specific information in WiFi systems that can be utilized in indoor positioning systems (IPSs). However, CFR-based IPSs can hardly achieve an accuracy at the centimeter level due to the limited bandwidth in WiFi systems. To achieve such accuracy using WiFi devices, we propose an IPS that fully harnesses the spatial diversity in multiple-input–multiple-output WiFi systems, which leads to a much larger effective bandwidth than the bandwidth of a WiFi channel. The proposed IPS obtains CFRs associated with locations-of-interest on multiple antenna links during the training phase. In the positioning phase, the IPS captures instantaneous CFRs from a location to be estimated and compares it with the CFRs acquired in the training phase via the time-reversal resonating strength with residual synchronization errors compensated. Extensive experiment results in an office environment with a measurement resolution of 5 cm demonstrate that, with a single pair of WiFi devices and an effective bandwidth of 321 MHz, the proposed IPS achieves detection rates of 99.91% and 100% with false alarm rates of 1.81% and 1.65% under the line-of-sight (LOS) and non-LOS (NLOS) scenarios, respectively. Meanwhile, the proposed IPS is robust against environment dynamics. Moreover, experiment results with a measurement resolution of 0.5 cm demonstrate a localization accuracy of 1–2 cm in the NLOS scenario.**

***Index Terms*—Channel frequency response (CFR), indoor localization, multiple-input–multiple-output (MIMO), time-reversal resonating strength (TRRS).**

I. Introduction

WIRELESS indoor positioning systems (IPSs) spawn numerous location-based indoor applications, such as campus-wide localization [1], targeted advertisement in supermarkets [2], and shopping mall navigations [3]. The IPSs often demand an accuracy in the sub-meter level, which cannot be achieved by the global positioning system (GPS) due to the severe attenuation of GPS signals indoor.

Manuscript received August 17, 2016; revised October 17, 2016; accepted November 6, 2016. Date of publication November 15, 2016; date of current version February 8, 2017.

C. Chen, F. Zhang, and K. J. R. Liu are with Origin Wireless Inc., Greenbelt, MD 20770 USA, and also with the Department of Electrical and Computer Engineering, University of Maryland at College Park, College Park, MD 20742 USA (e-mail: chen.chen@originwireless.net; feng.zhang@originwireless.net; ray.liu@originwireless.net).

Y. Chen was with Origin Wireless Inc., Greenbelt, MD 20770 USA. He is now with the University of Electronic Science and Technology of China, Chengdu 611731, China (e-mail: eecyan@uestc.edu.cn).

Y. Han and H.-Q. Lai are with Origin Wireless Inc., Greenbelt, MD 20770 USA (e-mail: yi.han@originwireless.net; quoc.lai@originwireless.net).

Digital Object Identifier 10.1109/JIOT.2016.2628713

The imperative demand on the accuracy leads to an extensive development of IPSs using a wide variety of wireless technologies [4]. Among them, WiFi-based approaches are promising candidates since they are built upon the WiFi networks widely available indoor. Many WiFi-based schemes exploit the location-specific fingerprints characterizing the propagation of electromagnetic waves for indoor spaces to facilitate indoor localization. Examples include the received signal strength indicator (RSSI) [5]–[7] and channel frequency response (CFR) [8]–[10]. Each of these IPSs consists of a training phase and a positioning phase. During the training phase, the IPS collects fingerprints associated with multiple locations-of-interest and stores the fingerprints into a database, while in the positioning phase, the IPS determines the location by comparing the instantaneous fingerprint against those stored in the database. Nevertheless, the localization performance of these IPSs is limited by the available bandwidth in WiFi systems, which is 20 or 40 MHz for 802.11n WiFi networks. The bandwidth limit introduces severe location ambiguity which leads to meter-level accuracy on average.

Recently, Wu *et al.* [11] presented the time-reversal IPS (TRIPS) to achieve a centimeter-level localization accuracy. TRIPS is a single-antenna IPS that uses channel impulse response (CIR) as the fingerprint. It leverages the time-reversal technique to achieve the high-resolution spatial-temporal focusing effect [12] for localization. With a bandwidth of 125 MHz on 5.4 GHz ISM band, TRIPS achieves a perfect detection rate with zero false alarm within an area of 0.9×1 m with a measurement resolution of 5 cm. The accuracy can be further driven to 1–2 cm. Despite its centimeter-level accuracy, TRIPS uses dedicated hardware and requires a large bandwidth to reduce location ambiguity.

Is it possible to achieve the centimeter-level accuracy on a WiFi platform by leveraging the TR technique? The answer is affirmative. Chen *et al.* [13], [14] harnessed the frequency diversity of WiFi systems by scanning multiple channels and formulates fingerprints by concatenating CFRs from these channels, leading to a perfect detection rate with zero false alarm with 5 cm measurement resolution. One drawback of this approach is the overhead of frequency hopping in acquiring CFRs from a large number of channels.

In this paper, we propose an IPS that leverages the spatial diversity on a multi-antenna WiFi device instead of the frequency diversity to achieve the centimeter-level accuracy. The proposed IPS optimally concatenates the available bandwidths of different antenna links to formulate a much

larger effective bandwidth. The IPS consists of two phases: 1) the training phase and 2) the positioning phase. During the training phase, the IPS captures CFRs from multiple locations-of-interest and then combines CFRs of different links into location fingerprints. In the positioning phase, the IPS obtains instantaneous CFRs and evaluates the TR focusing effect quantitatively by the time-reversal resonating strength (TRRS) between the instantaneous CFRs and those in the training phase. Realizing that the residual synchronization errors are inevitable in WiFi systems, we develop an algorithm to mitigate the impact of such errors in the computations of TRRS. Finally, the IPS determines the locations based on the TRRS.

We conduct extensive experiments in an office environment using a single pair of off-the-shelf WiFi devices to illustrate that the proposed IPS can achieve detection rates of 99.91% and 100%, while triggering negligible false alarm rates of 1.81% and 1.65% under line-of-sight (LOS) and non-LOS (NLOS) scenarios, respectively, for locations with a unit distance of 5 cm. We also show that the proposed IPS is robust against environment dynamics. Moreover, experiment results with a unit distance of 0.5 cm demonstrate that 1–2 cm accuracy is achievable with the proposed IPS. To the best of our knowledge, this is the first work that achieves 1–2 cm localization accuracy under NLOS scenarios using a single pair of off-the-shelf WiFi devices leveraging spatial diversity.

The main contributions of this paper can be summarized as follows.

1) We present the concept of effective bandwidth as a measure of exploitable diversities for localization.
2) We propose a robust algorithm that compensates the inevitable synchronization errors in WiFi transceivers when calculating the TRRS for each WiFi link. Then, it fuses the TRRS from different WiFi links via a weighted average scheme, which significantly reduces the location ambiguity caused by the bandwidth limit in WiFi systems.
3) We conduct extensive experiments in a typical office environment with dynamics introduced by human activities as well as the movement of objects such as furniture and doors. The experiment results demonstrate that the proposed IPS achieves centimeter-level accuracy and it is robust against environment dynamics.

The rest of this paper is organized as follows. In Section II, we present a literature survey on the indoor localization schemes relevant to the proposed IPS. In Section III, we introduce the TR technique and the channel estimation in multiple-input–multiple-output (MIMO)-OFDM WiFi systems. In Section IV, we elaborate on the localization algorithm for the IPS. In Section V, we demonstrate the experiment results. Finally, the conclusions are drawn in Section VI.

II. Related Work

In this section, we sample a few wireless indoor localization systems from the rich literature with high correlation with the proposed IPS. Based on their principles, these schemes can be further categorized into two classes: triangulation and fingerprinting [4].

A. Triangulation

Triangulation-based schemes utilize the geometric properties to localize the device using several anchors with known coordinates in the space. These schemes can be further classified into *lateration-based* and *angulation-based*.

1) Lateration: Lateration-based schemes measure the distances from the device to at least three anchors to facilitate triangulation. The distance is generally inferred from other information available in the wireless network relevant to the LOS path, such as RSSI, time of arrival (TOA), time difference of arrival (TDOA), and round-trip time-of-flight (RTOF). RSSI-based approaches estimate the distances between device and anchors based on the received signal strength via the free-space path-loss model or its variants which take the attenuation due to walls and ceilings into consideration. SpotON [15] uses the RFID technology for indoor localization. A SpotON tag measures the intertag distances using the RSSI values associated with the received tag. LANDMARC deploys extra fixed reference tags for calibration to improve the RFID localization accuracy [16]. Nevertheless, the high heterogeneity of indoor spaces give rise to strong NLOS components which complicates and degrades the efficacy of the path-loss model. Methods based on TOA, TDOA, and RTOF [17]–[21] suffer in a strong NLOS environment as well since the LOS component can hardly be discerned from the multipath profile. Moreover, the schemes proposed in [19]–[21] use ultra-wideband transmission to obtain a highly accurate timing resolution and thus require dedicated hardware which incurs additional cost in deployment.

2) Angulation: Angulation-based schemes calculate the angle of arrival (AOA) of a signal arrived at several anchors and formulate intersections of multiple spheres to pinpoint the device. Xiong and Jamieson [22] presented ArrayTrack, a phased antenna array composed by multiple access points (APs) with their initial phases synchronized by calibration. Each AP is built by stitching two customized WARP radios together with four omnidirectional antennas and is capable of AOA estimation utilizing the widely used MUSIC algorithm [23]. The mean accuracy reaches 107 cm with three APs and can be further improved to 57 cm by introducing an additional antenna for each AP. When all six APs are working simultaneously, the localization accuracy reaches 31 cm. Gjengset *et al.* [24] implemented the Phaser system with a high resemblance to ArrayTrack, except that two off-the-shelf WiFi cards are stitched together in Phaser to replace the two dedicated WARP radios utilized in ArrayTrack.

One drawback of ArrayTrack and Phaser is that phase calibration must be conducted for each AP to synchronize the initial phases between different antennas whenever the AP is powered on since the oscillators would locked onto unknown random phases. On the other hand, they are only accurate when the device has a direct link to at least one AP and thus multiple APs are needed in general. Last but not least, ArrayTrack requires specialized hardware, and Phaser makes physical modifications to the APs by stitching two of them together using a cable.

3) Lateration Combined With Angulation: More recently, Kotaru *et al.* [25] presented SpotFi that fuses both lateration

and angulation techniques. SpotFi performs spatial smoothing on the correlation matrix of CFRs and applies 2-D MUSIC algorithm to estimate the AoA and ToF of different multipath components jointly. Then, SpotFi identifies the LOS path by performing clustering on the assembled estimations from multiple packets. Finally, by combining the AoA estimation with the RSSI values from multiple APs, SpotFi determines the location via solving a nonconvex optimization problem. SpotFi achieves a median accuracy of 1.9, 0.8, and 0.6 m with 3, 4, and 5 APs, respectively, when the LOS path exists between the device and a majority of the APs, and the error increases to 1.6 m when only one or two APs have decent LOS paths to the device. Like ArrayTrack and Phaser, SpotFi relies on the assumption that at least one AP can establish LOS link with the device. Also, the computation complexity of SpotFi is intense due to the 2-D MUSIC algorithm, clustering, and solving the nonconvex optimization problem.

B. Fingerprinting

Fingerprinting-based approaches collect location-specific fingerprints at different locations-of-interest in the offline training phase and compares instantaneous fingerprints against those obtained in the training phase in the online positioning phase. Youssef and Agrawala [6] utilized RSSI from multiple APs as the fingerprints in the training phase and calculate the probability of the candidate locations in the online phase. The achievable accuracy is 1.4 m in 90% of the time. Sen *et al.* [8] proposed PinLoc that achieves a mean detection rate of 90% across 50 1 m $\times$ 1 m spots with multiple APs with less than 7% mean false alarm rate. The CFRs collected from each 1 m $\times$ 1 m spot is modeled as random vectors following the distribution of mixture Gaussian. Then, PinLoc uses variational Bayesian inference to partition the CFRs of every 1 m $\times$ 1 m spot into clusters with the centroid of each cluster as the representative CFR. Then, with a probabilistic measure, PinLoc evaluates the possibility of the instantaneous CFR in the online phase coming from each of the 1 m $\times$ 1 m spots for localization. However, they are unable to reach the centimeter-level accuracy since they find that multiple locations in a room may exhibit identical fingerprints. This can be justified by the fact that only 20 MHz of bandwidth is utilized for CFR fingerprinting, which increases the location ambiguity.

Utilizing the spatial diversity in MIMO WiFi systems can further bolster the IPS performances. The fine-grained indoor fingerprinting system (FIFS) proposed in [9] formulates the compressed fingerprints by aggregating CFR amplitudes of different antenna links. It achieves an accuracy of 1.1 m under 2×2 MIMO configuration. The accuracy of FIFS is improved to 0.95 m in [10] by incorporating the phase information contained in the CFRs as well. However, centimeter-level accuracy cannot be achieved in the two schemes as the spatial diversity are not fully harnessed in an optimal way.

III. Preliminaries

In this section, we briefly introduce the TR technique and the channel estimation schemes in WiFi systems.

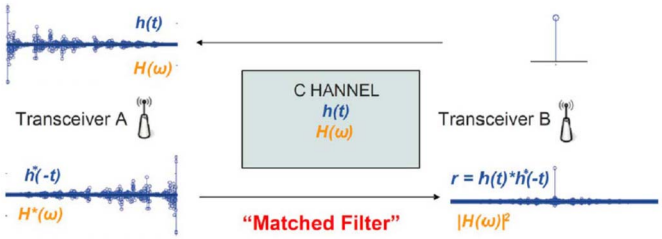

Fig. 1. Simple TR wireless communication system.

A. Time-Reversal

TR is a signal processing technique that mitigates the phase distortion of a signal filtered by a linear time-invariant (LTI) system. It leverages the fact that the phase distortion can be removed at a particular time instance when the LTI system $h(t)$ is combined with its time-reversed and conjugated counterpart $h^*(-t)$. The development of TR can be dated back to the 1950s when Bogert uses TR technique to correct a slow picture transmission system delay distortion [26]. Later, Kormylo and Jain [27] utilized TR in the design of zero-phase digital filters, as the signal is processed in both causal and reverse causal direction to remove the phase distortion.

The physical channel can be regarded as LTI if it is inhomogeneous and invertible. When such conditions hold, TR technique can refocus the energy of signal waves at a particular spatial location and a specific time, known as the spatial-temporal focusing effect. This effect is verified experimentally in the field of ultrasonics, acoustics, and electromagnetism [12], [28]–[30]. More recently, TR is applied to the broadband wireless communication systems [31].

The concept of TR communication is illustrated in Fig. 1. When transceiver A intends to send information to transceiver B, transceiver B sends a probing signal to transceiver A, which is termed as the *channel probing phase*. Upon reception of the probing signal, transceiver A extracts the CIR, time-reverses, and takes conjugate to generate a signature. In the second phase, termed as the *TR transmission phase*, transceiver A convolves the transmitted symbols with the signature and sends to transceiver B. The channel acts as a matched filter during the transmission due to the time-reversal operation. The TR focusing peak can be observed at a specific time instance at transceiver B, the source location of the channel probing phase. It is by virtue of the TR focusing effect at the intended location that TR technique is employed successfully in indoor positioning applications [11].

B. Channel Estimation in MIMO-OFDM

Assume an MIMO-OFDM system with N_t transmitting antennas and N_r receiving antennas, and denote the CIR between transmitting antenna (TX) n_t and receiving antenna (RX) n_r as $h_{n_t,n_r}[\ell]$ where ℓ runs from 0 to $L_{n_t,n_r}-1$, and L_{n_t,n_r} is the number of multipath components between TX n_t and RX n_r. To facilitate timing/frequency synchronization and channel estimation, TX n_t sends a training sequence $x_{n_t}[n]$ composed by several short training fields (STFs), guard intervals (G), and N_t long training fields (LTFs). The nth sample

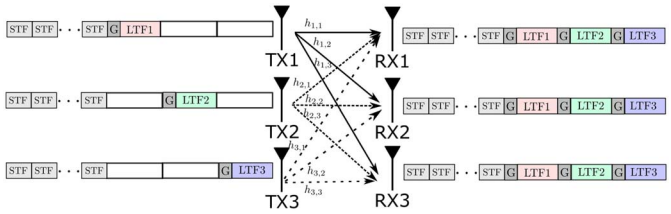

Fig. 2. Channel estimation in MIMO-OFDM WiFi system.

of the received signal at RX n_r can be expressed as

$$y_{n_r}[n] = \sum_{n_t=1}^{N_t} \sum_{l=0}^{L_{n_t,n_r}-1} h_{n_t,n_r}[l] x_{n_t}[n-l] + w_{n_r}[n] \tag{1}$$

where $w_{n_r}[n]$ is the channel noise at RX n_r. Assisted by the STFs, RX n_r detects the starting position of the first LTF. Then, it performs N-point fast Fourier transform (FFT) on all LTFs. After discarding the null subcarriers, the frequency domain representation of $y_{n_r}[n]$ on the kth usable subcarrier associated with the ith LTF takes the form

$$Y_{i,n_r}[u_k] = \sum_{n_t=1}^{N_t} H_{n_t,n_r}[u_k] X_{i,n_t}[u_k] + W_{i,n_r}[u_k] \tag{2}$$

where u_k is the index for the kth subcarrier with $k = 1, 2, \ldots, N_u$, N_u is the number of usable subcarriers, $H_{n_t,n_r}[u_k]$ is the frequency domain representation of $\{h_{n_t,n_r}[\ell]\}_{\ell=0,1,\ldots,L_{n_t,n_r}-1}$ on the kth subcarrier, $X_{i,n_t}[u_k]$ is the frequency domain representation of $x_{n_t}[n]$ with n in the range of the ith LTF on the kth subcarrier, and $W_{i,n_t}[u_k]$ is the frequency domain noise of the ith LTF on the kth subcarrier.

Fig. 2 illustrates the channel estimation procedure in MIMO-OFDM WiFi systems [32]. The TX transmits LTFs alternatively such that at any given time instance, only one TX is sending the LTF. Thus, $X_{i,n_t}[u_k]$ is expressed by

$$X_{i,n_t}[u_k] = X[u_k]\mathbf{1}(i = n_t) \tag{3}$$

where $\mathbf{1}(x)$ is the indicator function. Substituting $X_{i,n_t}[u_k]$ back into (2) gives

$$Y_{i,n_r}[u_k] = \big[H_{i,n_r}[u_k]X[u_k] + W_{i,n_r}[u_k]\big]\mathbf{1}(i = n_t). \tag{4}$$

Assuming that the frequency domain noise follows a Gaussian distribution, the CFR $H_{n_t,n_r}[u_k]$ can be estimated in the least-square sense using:

$$\hat{H}_{n_t,n_r}[u_k] = \frac{Y_{n_t,n_r}[u_k]}{X[u_k]} = H_{n_t,n_r}[u_k] + \frac{W_{n_t,n_r}[u_k]}{X[u_k]}. \tag{5}$$

Equation (5) depicts $H_{n_t,n_r}[u_k]$ in the ideal case. In practice, the WiFi receivers suffer from the carrier frequency offset (CFO), sampling frequency offset (SFO), and symbol timing offset (STO) caused by the mismatches of analog and digital components between the transmitters and receivers. Although WiFi receivers perform synchronization, the residual synchronization errors cannot be neglected. Meanwhile, the phase locked loops (PLLs) at the WiFi receivers produce random common phase offsets (CPOs). These additional errors must be considered since they are random in nature and introduce severe uncertainties into the CFRs.

In the presence of the aforementioned synchronization errors, the channel estimation at RX n_r takes the form [33]

$$\begin{aligned}\hat{H}_{n_t,n_r}[u_k] = {} & H_{n_t,n_r}[u_k] e^{j\nu_{n_r}} \\ & \times e^{j2\pi\left(\alpha_{n_t}(\Delta s_{n_r}, \Delta\omega_{n_r}) + \epsilon_{n_t}(\Delta\psi_{n_r}, \Delta\eta_{n_r})u_k\right)} \\ & + U_{n_t,n_r}[u_k]\end{aligned} \tag{6}$$

where $U_{n_t,n_r}[u_k]$ is the estimation noise between TX n_t and RX n_r, ν_{n_r} is the CPO at RX n_r, Δs_{n_r} is the reference absolute time of the detected frame starting point after timing synchronization using STFs, $\Delta\omega_{n_r}$ is the normalized residual SFO at RX n_r given as $(\Delta f_r)/(NT_s)$, where Δf_r is the residual CFO at RX n_r, $\Delta\psi_{n_r}$ is the STO at RX n_r, and $\Delta\eta_{n_r}$ is the residual SFO at RX n_r expressed as $(T_s' - Ts)/(T_s)$ where T_s and T_s' are the sampling intervals at the TX and RX, respectively. The initial and linear phase distortions are denoted by $\alpha_{n_t}(\Delta s_{n_r}, \Delta\omega_{n_r})$ and $\epsilon_{n_t}(\Delta\psi_{n_r}, \Delta\eta_{n_r})$ which take the form

$$\alpha_{n_t}\big(\Delta s_{n_r}, \Delta\omega_{n_r}\big) = \frac{\big(\Delta s_{n_r} + (i-1)N_s + N_G + \frac{N}{2}\big)\Delta\omega_{n_r}}{N} \tag{7}$$

$$\epsilon_{n_t}\big(\Delta\psi_{n_r}, \Delta\eta_{n_r}\big) = \frac{\Delta\psi_{n_r} + \big((i-1)N_s + N_G + \frac{N}{2}\big)\Delta\eta_{n_r}}{N}. \tag{8}$$

Here, N_G is the number of samples of the guard interval, and $N_s = N_G + N$ is the total number of samples of one OFDM block.

To illustrate the impact of phase distortions on CFRs, we show the normalized amplitudes and phases of 200 CFRs captured within 4 s in Fig. 3(a) and (b). Despite the consistency in the normalized amplitudes, the variations in the phases caused by the aforementioned initial and linear phase distortions differ for different packets and must be compensated.

IV. Algorithm Design

A. Calculating TRRS for Each Link

Given two CIRs $\hat{\mathbf{h}} = [\hat{h}[0], \hat{h}[1], \ldots, \hat{h}[L-1]]^{\mathsf{T}}$ and $\hat{\mathbf{h}}' = [\hat{h}'[0], \hat{h}'[1], \ldots, \hat{h}'[L-1]]^{\mathsf{T}}$, where $(\cdot)^{\mathsf{T}}$ represents the transpose operator, the TRRS between them is given by [11]

$$\gamma_{\mathsf{CIR}}\Big[\hat{\mathbf{h}}, \hat{\mathbf{h}}'\Big] = \frac{\left(\max_i \left|\big(\hat{\mathbf{h}} * \hat{\mathbf{g}}\big)[i]\right|\right)^2}{\Big\langle\hat{\mathbf{h}}, \hat{\mathbf{h}}\Big\rangle\big\langle\hat{\mathbf{g}}, \hat{\mathbf{g}}\big\rangle} \tag{10}$$

where $*$ stands for the linear convolution, $\hat{\mathbf{g}}$ is the time-reversed and conjugate counterpart of $\hat{\mathbf{h}}'$. $\langle\mathbf{x}, \mathbf{y}\rangle$ is the inner product operator between vector $\mathbf{x}$ and $\mathbf{y}$ given as $\mathbf{x}^{\dagger}\mathbf{y}$, and $(\cdot)^{\dagger}$ is the Hermitian operator. In (10), taking maximum over all possible i in the calculation of $\gamma_{\mathsf{CIR}}[\hat{\mathbf{h}}, \hat{\mathbf{h}}']$ essentially mitigates the linear phase distortions caused by STO. Meanwhile, taking the absolute value on the numerator as shown in (10) eliminates the initial phase distortions. However, the residual SFO is uncompensated.

Since cross correlation in time domain is equivalent to inner product in frequency domain, we redefine the TRRS between two CFRs in the frequency domain by extending (10) into MIMO-OFDM systems. Here, we assume two CFRs denoted as $\hat{\mathbf{H}}_{n_t,n_r}$ and $\hat{\mathbf{H}}'_{n_t,n_r}$ between TX n_t and RX n_r.

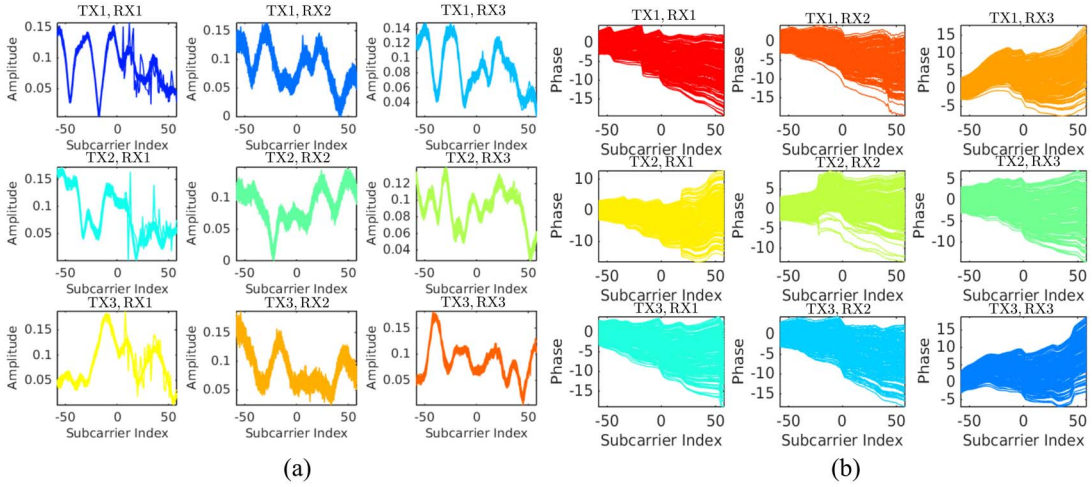

Fig. 3. Snapshot of CFRs of 9 links in a 3 × 3 MIMO-OFDM system collected in 4 s. (a) Normalized amplitudes. (b) Unwrapped phases.

For convenience, we define the *link index* $d = (n_t - 1)N_r + n_r$.[1] Then, $\hat{\mathbf{H}}_d$ is expressed as

$$\hat{\mathbf{H}}_d = \left[\hat{H}_d[u_1] \quad \hat{H}_d[u_2] \quad \cdots \quad \hat{H}_d[u_k] \quad \cdots \quad \hat{H}_d[u_{N_u}]\right]^{\mathsf{T}}. \tag{11}$$

Similar definition applies for $\hat{\mathbf{H}}'_d$. Given $\hat{\mathbf{H}}_d$ and $\hat{\mathbf{H}}'_d$, we define the TRRS on link d as

$$\overline{\phi}_d = \frac{\max\limits_{\epsilon} \left| \sum_{k=1}^{N_u} \hat{H}_d[u_k]\hat{H}'^{*}_d[u_k]e^{j\epsilon u_k} \right|^2}{\Lambda_d \Lambda'_d} \tag{12}$$

where

$$\Lambda_d = \langle \mathbf{H}_d, \mathbf{H}_d \rangle, \quad \Lambda'_d = \langle \mathbf{H}'_d, \mathbf{H}'_d \rangle \tag{13}$$

are the *channel energies* for $\mathbf{H}_d$ and $\mathbf{H}'_d$, respectively. As can be seen from by the numerator of (12), the effect of both STO and SFO are alleviated by searching ϵ in the linear term $e^{j\epsilon u_k}$, while the impact of initial phase distortion is totally eliminated by taking the absolute value in (12).

Calculating $\overline{\phi}_d$ requires an accurate estimation of ϵ which can be very inefficient if brute-force fine-grained search is performed. To obtain ϵ efficiently, we employ an FFT with size N_{ser}, leading to a searching resolution of $2\pi/N_{\mathsf{ser}}$ in the range of $[0, 2\pi)$ for $\overline{\phi}_d$. The algorithm is summarized into Algorithm 1.

The phase correction as shown as step 8 in Algorithm 1 differs significantly from the phase sanitization scheme in [8]. The phase sanitization scheme performs phase unwrapping on the CFR phases, which is error-prone in the presence of phase noise. Moreover, it totally eliminates the linear phase contained in the unwrapped CFR phases via the least-square estimation, which might also remove useful information about the environment as the side effect.[2] On the other hand, the proposed phase correction step estimates ϵ by matching two CFRs using FFT and does not perform phase unwrapping. Therefore, the proposed method is more robust against noise.

[1]For instance, in a 3 × 3 MIMO system, the link between TX antenna 2 and RX antenna 1 is labeled as link 4.

[2]The reflectors in the environment also introduce linear phase shifts into the frequency-domain CFRs.

Algorithm 1 Calculating the TRRS $\overline{\phi}_d$ for Link d

Input: $\{\hat{H}_d[u_k]\}_{k=1,2,\ldots,N_u}$, $\{\hat{H}'_d[u_k]\}_{k=1,2,\ldots,N_u}$
Output: $\overline{\phi}_d$

1: Intializing $\Lambda_d = 0$ and $\Lambda'_d = 0$
2: **for** $k = 1, 2, \ldots, N_u$ **do**
3: Calculating $\hat{G}[u_k] = \hat{H}_d[u_k]\hat{H}'^{*}_d[u_k]$
4: Calculating $\Lambda_d = \Lambda_d + \hat{H}_d[u_k]\hat{H}^{*}_d[u_k]$
5: Calculating $\Lambda'_d = \Lambda'_d + \hat{H}'_d[u_k]\hat{H}'^{*}_d[u_k]$
6: **end for**
7: Appending $(N_{\mathsf{ser}} - N_u)$ zeros at the end of $\{\hat{G}[u_k]\}_{k=1,2,\ldots,N_u}$ if $N_{\mathsf{ser}} \geq N_u$. Otherwise, discarding the last $(N_u - N_{\mathsf{ser}})$ entries of $\{\hat{G}[u_k]\}_{k=1,2,\ldots,N_u}$.
8: Performing an N_{ser}-point FFT on $\{\hat{G}[u_k]\}_{k=1,2,\ldots,N_u}$, which leads to $\{g[n]\}_{n=1,2,\ldots,N_{\mathsf{ser}}}$ given as

$$g[n] = \sum_{k=1}^{N_{\mathsf{ser}}} \hat{G}[u_k] e^{-j\frac{2\pi n(k-1)}{N_{\mathsf{ser}}}}. \tag{14}$$

9: Calculating $\overline{\phi}_d = \frac{\max\limits_{n=1,2,\ldots,N_{\mathsf{ser}}} |g[n]|^2}{\Lambda_d \Lambda'_d}$.
10: **return** $\overline{\phi}_d$

B. Fusing TR Resonating Strength of Different Links

In a MIMO-OFDM WiFi system, the combined CFR consisting of the CFRs captured from different links can be expressed by

$$\hat{\mathbb{H}} = \left[\hat{\mathbf{H}}_1^{\mathsf{T}} \quad \hat{\mathbf{H}}_2^{\mathsf{T}} \quad \cdots \quad \hat{\mathbf{H}}_d^{\mathsf{T}} \quad \cdots \quad \hat{\mathbf{H}}_D^{\mathsf{T}}\right]^{\mathsf{T}} \tag{15}$$

with $\hat{\mathbb{H}}'$ defined similarly, we calculate $\{\overline{\phi}_d\}_{d=1,2,\ldots,D}$ and fuse them together into the combined TRRS $\gamma[\hat{\mathbb{H}}, \hat{\mathbb{H}}']$, expressed by

$$\gamma\left[\hat{\mathbb{H}}, \hat{\mathbb{H}}'\right] = \left(\sum_{d=1}^{D} \omega_d \sqrt{\overline{\phi}_d}\right)^2 \tag{16}$$

where

$$\omega_d = \frac{\sqrt{\Lambda_d \Lambda'_d}}{\sqrt{\sum_{d=1}^{D} \Lambda_d} \sqrt{\sum_{d=1}^{D} \Lambda'_d}} \tag{17}$$

is the weight for the dth link. The intuition behind the choice of ω_d lies in that given identical channel noise on different link pairs, those link pairs with higher channel energy products are more robust against noise and thus should be allocated a higher weight in calculating the combined TRRS. The denominator of ω_d scales $\gamma[\hat{\mathbb{H}}, \hat{\mathbb{H}}']$ into the range of $[0, 1]$.

C. Effective Bandwidth

Since we fully utilize the information contained in $\hat{\mathbb{H}}$ and $\hat{\mathbb{H}}'$ in computing the combined TRRS $\gamma[\hat{\mathbb{H}}, \hat{\mathbb{H}}']$, we achieve an effective bandwidth W_e of

$$W_e = \frac{DN_uB}{N} \tag{18}$$

where B is the bandwidth per link. For 802.11n WiFi systems, B can be as large as 40 MHz. Notice that, the effective bandwidth is different from the physical channel bandwidth allocated to a WiFi channel. In this paper, the effective bandwidth is used as a metric to quantify the available resources in a fingerprint-based IPS that can be harnessed for localization. A larger effective bandwidth generally leads to a better localization performance in terms of the detection rates and the false alarm rates and thus can provide an insight into the performance of the IPS.

D. Localization Using Combined TRRS

The proposed IPS consists of a training phase and a positioning phase, which are elaborated in the subsequent part of this section.

1) Training Phase: During the training phase, we collect R CFR realizations from each of the L locations-of-interest. The $L \times R$ CFRs are stored into the CFR database denoted as $\mathbf{D}_{\text{train}}$. The ith column of $\mathbf{D}_{\text{train}}$ is given by $\hat{\mathbb{H}}_i$, with $\hat{\mathbb{H}}_i$ shown as (15), and i is the *training index*. Denote the realization index as r and the location index as ℓ, the training index i can be mapped from (r, ℓ) as $i = (\ell - 1)R + r$.

2) Positioning Phase: The problem of determining the device location can be cast into an multihypothesis testing problem. More specifically, assume that we collect an instantaneous CFR $\hat{\mathbb{H}}'$ from a location ℓ' to be estimated. Then, we calculate the combined TRRS between each CFR in $\mathbf{D}_{\text{train}}$ and $\hat{\mathbb{H}}'$ shown as (16), which leads to $\{\gamma[\hat{\mathbb{H}}_i, \hat{\mathbb{H}}']\}_{i=1,2,\ldots,\text{LR}}$. After that, we take the maximum of the multiple combined TRRS evaluated at the same training location ℓ but with different realization index r, expressed by

$$\gamma_\ell = \max_{\substack{i=(\ell-1)R+r \\ r=1,2,\ldots,R}} \gamma\left[\hat{\mathbb{H}}_i, \hat{\mathbb{H}}'\right]. \tag{19}$$

Now, we define a total of $L + 1$ hypothesis $\mathcal{H}_0, \mathcal{H}_1, \mathcal{H}_2, \ldots, \mathcal{H}_\ell, \ldots, \mathcal{H}_L$, where $\mathcal{H}_{\ell,\ell\neq 0}$ stands for the hypothesis that the device is located at location ℓ in the training phase, and $\mathcal{H}_0$ represents the hypothesis that the device is located at an unknown location excluded from the training phase. We determine that $\mathcal{H}_{\ell,\ell\neq 0}$ is true, i.e., the device is located at the ℓth location in the training database, if the following two conditions are satisfied:

$$\gamma_\ell \geq \Gamma, \ \gamma_\ell = \max_{\ell'=1,2,\ldots,L} \gamma_{\ell'} \tag{20}$$

where Γ is a threshold in the range of $[0, 1]$. On the other hand, if $\gamma_\ell \leq \Gamma, \ \forall \ell = 1, 2, \ldots, L$, we determine that $\mathcal{H}_0$ is true, i.e., we are unable to localize the device since there is no match between the instantaneous CFRs and those in $\mathbf{D}_{\text{train}}$.

3) Configuration of Threshold: The IPS performance is significantly affected by Γ. A well-chosen Γ leads to a high detection rate and incurring negligible false alarm rate. The detection rate, denoted by $P_D(\Gamma)$, characterizes the probability that the IPS successfully determines the correct locations of the device under Γ, while the false alarm rate, denoted as $P_F(\Gamma)$, captures the possibility that the IPS makes incorrect decisions on the device location under Γ.

With a constraint imposed on the detection rate as $P_{D,0}$ and the false alarm rate as $P_{\text{FA},0}$, the IPS learns Γ automatically from CFRs in $\mathbf{D}_{\text{train}}$ in the training phase. First of all, the IPS computes the TRRS matrix $\mathbf{R}$ based on all CFRs in the training database $\mathbf{D}_{\text{train}}$, with the (i, j)th entry of $\mathbf{R}$ given by $\gamma[\mathbb{H}_i, \mathbb{H}_j]$, where $\mathbb{H}_i$ and $\mathbb{H}_j$ are the ith and jth CFR captured in the training phase, respectively. Notice that $[\mathbf{R}]_{i,i} \triangleq 1$. Then, the IPS evaluates $(P_D(\Gamma), P_{\text{FA}}(\Gamma))$ for a variety for Γ, until it finds a specific $\Gamma^\star$ such that $P_D(\Gamma^\star) \geq P_{D,0}$ and $P_{\text{FA}}(\Gamma^\star) \leq P_{\text{FA},0}$. Finally, $\Gamma^\star$ is utilized as the threshold in the positioning phase shown in (20).

V. Experiment Results

A. Experiment Settings

1) Environment: The experiments are conducted in a typical office in a multistorey building. The indoor space is occupied by desks, computers, chairs, and shelves.

2) Devices: We build several prototypes equipped with off-the-shelf WiFi devices. Each WiFi device is equipped with three omnidirectional antennas to support 3×3 MIMO configuration. Based on functionalities, these WiFi devices can be further classified as APs and stations (STAs). The center frequency of each AP is configured as 5.24 GHz. The prototype is shown in Fig. 5.

3) Details of Experiments: We conduct seven experiments in total to assess the performance of the proposed IPS with settings illustrated in Fig. 4. Experiments (Exps.) 1–4 are conducted under a measurement resolution of 5 cm to analyze the performance under a static and a dynamic environment with details given below.

- Exp. 1: It investigates the localization performance of the proposed algorithm with a 5 cm resolution. The WiFi devices are placed under the LOS setting, denoted as Exp. 1a, as well as the NLOS setting, denoted as Exp. 1b. For each experiment, we measure the CFRs of 100 locations on a measurement structure as shown in Fig. 5. The measurement resolution is $d = 5$ cm. For each location, ten CFRs are measured.
- Exp. 2: Light sheds on the impact of human activities. One participant is asked to walk randomly in the vicinity of the STA on the measurement structure with $d = 5$ cm as the unit distance. The distances between the participant and the STA range from 8 to 10 feet. The AP is placed at the same NLOS

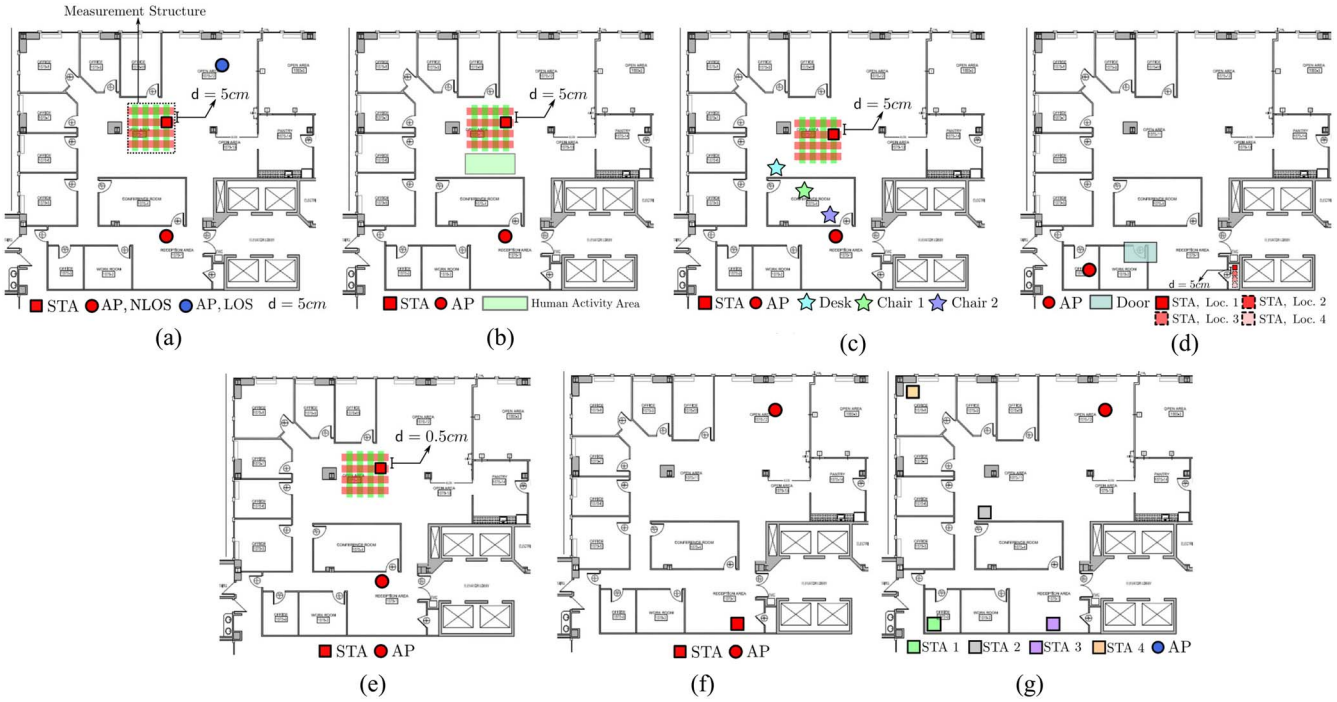

Fig. 4. Setups for the experiments. (a)–(g) Exps. 1–7.

position as in Exp. 1b. CFRs from 40 different locations on the structure are collected, with ten CFRs per location.

Exp. 3: It analyzes the localization performance when we introduce environment dynamics via moving the furniture in the office. We measure a total of five locations on the measurement structure with a resolution of 5 cm. For each location, we first measure ten CFRs without furniture movement, followed by another ten CFRs measured after we move the position of a desk near the measurement structure. Then, we measure ten CFRs after we move a chair in the conference room and the last ten CFRs after we move another chair in the conference room.

Exp. 4: It studies the impact of door opening/closing on the localization performance. The AP is placed in an office room, with STA located in a closet near the entrance of the office suite. The direct link between the AP and the STA is blocked by two concrete walls. Then, a participant is asked to open and close the door of a room in the middle between the AP and STA. CFRs from four positions in the closet are captured with ten CFRs per location for each door status.

On the other hand, Exps. 5–7 study several important aspects of the proposed IPS, where as follows.

Exp. 5: It studies the achievable accuracy of proposed IPS. The STA is placed at the same measurement structure with Exp. 1, but with a much finer resolution with $d = 0.5$ cm. CFRs from a total of 400 locations on the grid points of a rectangular area are measured, with five CFRs per location.

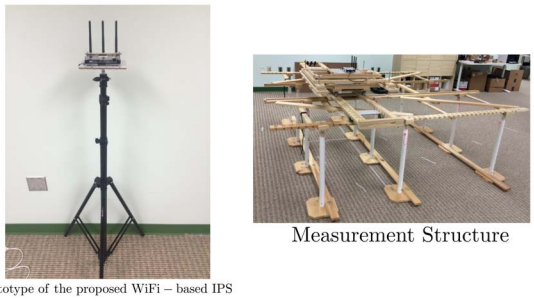

Fig. 5. WiFi prototype for the proposed IPS and the measurement structure used in the experiments.

Exp. 6: It studies the effect of the variations in the synchronization parameters. The positions of the AP and the STA are fixed, and we turn on and off the power of the AP to enforce the reinitialization the PLL at the AP. Thus, the synchronization parameters discussed in Section III-B also changes. The power cycling is repeated 20 rounds with ten CFRs for each round.

Exp. 7: It analyzes the long-term behavior of the IPS. One AP and four STAs are deployed in the office with positions shown in Fig. 4(g). The CFRs are collected every 10 min from the four STAs. The IPS is kept running for 631 h (26 days) continuously. For each measurement, we collect five CFRs from each STA. In the 26 days of measurement, the office is fully occupied by around ten people during weekdays and occasionally occupied during weekends. Also, the furniture is moved randomly every day.

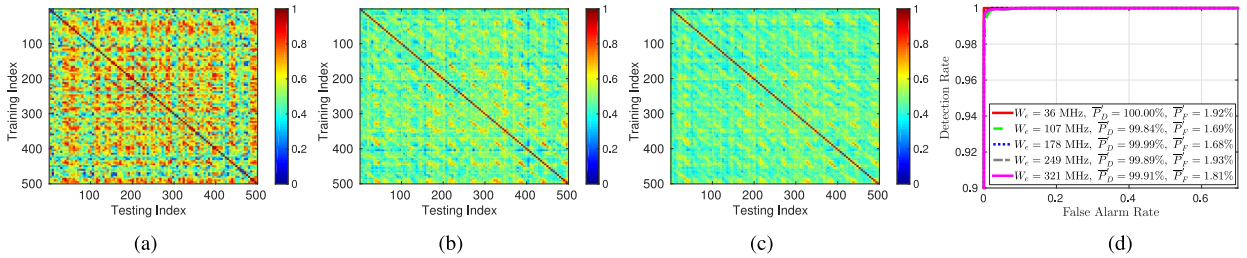

Fig. 6. Results of Exp. 1a under LOS. (a) $W_e = 36$ MHz. (b) $W_e = 178$ MHz. (c) $W_e = 321$ MHz. (d) ROC curve.

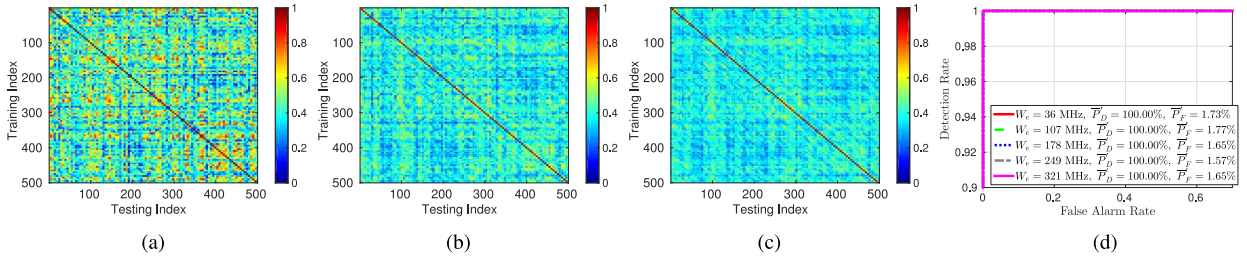

Fig. 7. Results of Exp. 1b under NLOS. (a) $W_e = 36$ MHz. (b) $W_e = 178$ MHz. (c) $W_e = 321$ MHz. (d) ROC curve.

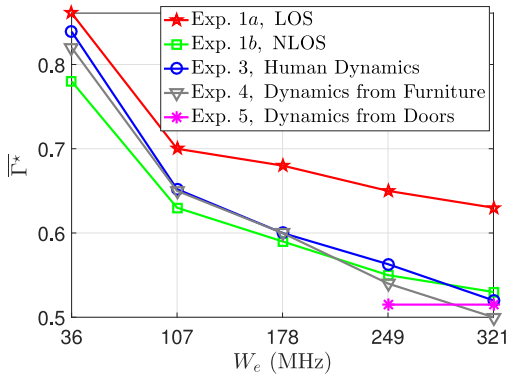

Fig. 8. $\overline{\Gamma^\star}$ under different W_e.

The effective bandwidths W_e in the experiments is calculated from (18) with $N_u = 114$, $N = 128$, and $D = 1, 2, 3, \ldots, 9$, with the maximum W_e as 321 MHz obtained by exploiting all available links under the 3×3 MIMO configuration, e.g., $D = 9$. In the performance evaluations, N_{ser} shown in Algorithm 1 is configured as 1024.

B. Metrics for Performance Evaluation

For Exps. 1–4, we evaluate the detection rate $P_D(\Gamma^\star)$ and the false alarm rate $P_{\text{FA}}(\Gamma^\star)$ under threshold $\Gamma^\star$. More specifically, we choose five out of the ten CFRs of each location randomly and consider them as the CFRs obtained in the training phase for each location-of-interest, which are assembled into the training database $\mathbf{D}_{\text{train}}$. The remaining five CFRs of each location are considered as the CFRs obtained in the positioning phase and are arranged into the testing database denoted by $\mathbf{D}_{\text{test}}$.

Using the scheme presented in Section IV, we calculate $P_D(\Gamma)$ and $P_{\text{FA}}(\Gamma)$ for $\Gamma \in [0, 1]$ based on the TRRS matrix $\mathbf{R}$ calculated from $\mathbf{D}_{\text{train}}$. By comparing $P_D(\Gamma)$ against $P_{\text{FA}}(\Gamma)$ under various Γ, we demonstrate the receiver operating characteristic (ROC) curve to highlight the tradeoffs between detection and false alarm. Then, we choose the minimum $\Gamma^\star$ that satisfies the objective $P_D(\Gamma^\star) \geq 95\%$, $P_{\text{FA}}(\Gamma^\star) \leq 2\%$ as the threshold. Lastly, we calculate the TRRS matrix $\mathbf{R}'$ from $\mathbf{D}_{\text{test}}$ and evaluates $P'_D(\Gamma^\star)$ and $P'_{\text{FA}}(\Gamma^\star)$ based upon $\mathbf{R}'$ and $\Gamma^\star$. To fully utilize the collected CFRs, we repeat this process five times by randomizing the selections of CFRs for the training phase and positioning phase. Finally, we compute the average of $\Gamma^\star$, $P'_D(\Gamma^\star)$, and $P'_{\text{FA}}(\Gamma^\star)$, denoted as $\overline{\Gamma^\star}$, $\overline{P}'_D$, and $\overline{P}'_{\text{FA}}$, respectively.

In Exp. 5, we illustrate the distribution of the TRRS on the measurement structure. In particular, we assemble the CFRs obtained from the middle point of the 10×10 cm rectangular grid into $\mathbf{D}_{\text{train}}$, and keep the CFRs of all locations into $\mathbf{D}_{\text{test}}$. Then, we compute the TRRS matrix $\mathbf{R}$ based on $\mathbf{D}_{\text{train}}$ and $\mathbf{D}_{\text{test}}$.

In Exp. 6, we build $\mathbf{D}_{\text{train}}$ with all CFRs, with $\mathbf{D}_{\text{test}}$ the same as $\mathbf{D}_{\text{train}}$. Thus, the TRRS matrix $\mathbf{R}$ encapsulates the impact of time-varying synchronization parameters on the localization performance.

In Exp. 7, for each STA, we construct $\mathbf{D}_{\text{train}}$ using the five CFRs collected in the first measurement, and keeps all CFRs measured at different time into $\mathbf{D}_{\text{test}}$. After calculating the TRRS matrix $\mathbf{R}$, we take the column average of $\mathbf{R}$, denoted as $\overline{\mathbf{R}}$, which represents the average TRRS between the CFR in $\mathbf{D}_{\text{train}}$ and those in $\mathbf{D}_{\text{test}}$ of every 10 min. Using $\overline{\mathbf{R}}$, we evaluate the detection rate and false alarm rate.

C. Performance Evaluation

1) Exp. 1a (LOS With 5 cm Resolution): In Fig. 6(a)–(c), we demonstrate the TRRS matrix $\mathbf{R}$ with different W_e under the LOS scenario. As we can see, increasing W_e shrinks the off-diagonal components of $\mathbf{R}$. In other words, a larger W_e alleviates the ambiguity among different locations. On the other

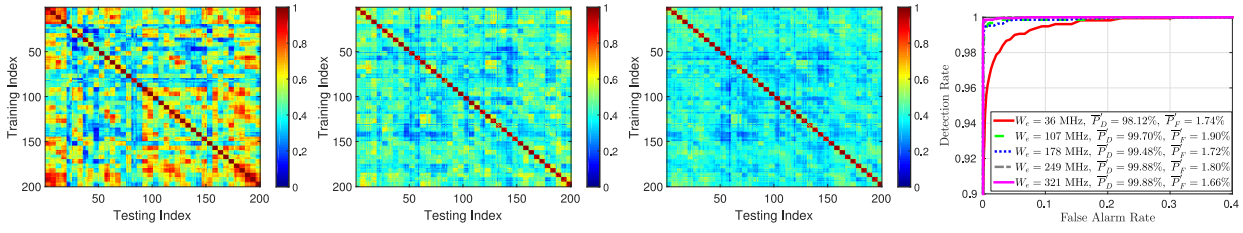

Fig. 9. Results of Exp. 2 with human dynamics. (a) $W_e = 36$ MHz. (b) $W_e = 178$ MHz. (c) $W_e = 321$ MHz. (d) ROC curve.

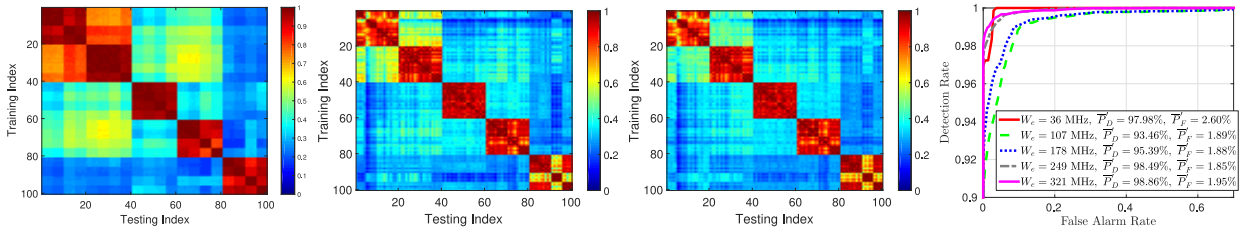

Fig. 10. Results of Exp. 3 with furniture movement. (a) $W_e = 36$ MHz. (b) $W_e = 178$ MHz. (c) $W_e = 321$ MHz. (d) ROC curve.

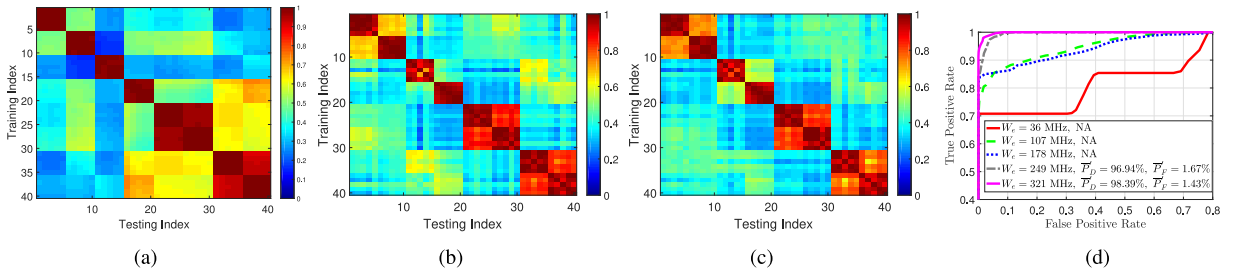

Fig. 11. Results of Exp. 4 with door effect. (a) $W_e = 36$ MHz. (b) $W_e = 178$ MHz. (c) $W_e = 321$ MHz. (d) ROC curve.

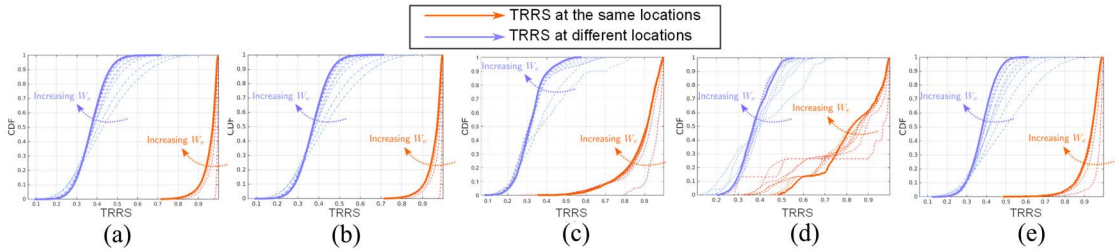

Fig. 12. Impact of W_e on the TRRS. (a) Exp. 1a, LOS under static environment. (b) Exp. 1b, NLOS under static environment. (c) Exp. 2, dynamic environment with human activities. (d) Exp. 3, dynamic environment with furniture movement. (e) Exp. 4, dynamic environment with door opening and closing.

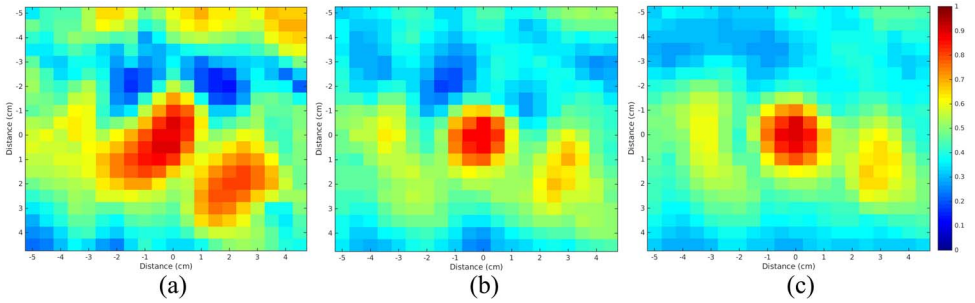

Fig. 13. Results of Exp. 5 under a measurement resolution of 0.5 cm. (a) $W_e = 36$ MHz. (b) $W_e = 178$ MHz. (c) $W_e = 321$ MHz.

hand, the TRRS values measured at the same location only degrades slightly and are still close to 1 with a large W_e. The net effect of using a large W_e is a larger margin between the TRRS calculated at the same location and among different locations, evidencing an enhanced location distinction. The ROC curve in Fig. 6(d) demonstrates that the IPS achieves

nearly perfect localization performance with $\overline{P}_D' \geq 99.84\%$ and $\overline{P}_{\text{FA}}' \leq 1.93\%$ under different W_e. When $W_e = 36$ MHz, we can achieve $\overline{P}_D' = 100\%$ and $\overline{P}_{\text{FA}}' = 1.92\%$, which implies that even there exists ambiguity among locations as shown in Fig. 6(a) when $W_e = 36$ MHz, we are able to find a good $\overline{\Gamma^\star}$ to distinguish different locations.

However, in general, the threshold $\overline{\Gamma^\star}$ is large when W_e is small. Therefore, under a small W_e, the IPS is highly sensitive to noise and deterioration of CFRs associated with different locations, e.g., when there exists significant environment dynamics due to human or object movement. On the other hand, $\overline{\Gamma^\star}$ is much smaller when W_e is large, which leaves a larger margin for noise and dynamics and thus improves the robustness of the proposed IPS. This is justified by Fig. 8, where we demonstrate $\overline{\Gamma^\star}$ under different W_e for Exp. 1a. It can be seen that a threshold as large as 0.86 is required when $W_e = 36$ MHz, which decreases as W_e increases. When $W_e = 321$ MHz, the threshold drops to 0.63.

2) Exp. 1b (NLOS With 5 cm Resolution): In Fig. 7(a)–(c), we show the TRRS matrix $\mathbf{R}$ with different W_e under the NLOS scenario. Comparing with Fig. 6(a)–(c), we see that the location ambiguity is lower for the NLOS scenario than the LOS scenario, indicating by the smaller TRRS values measured between different locations. This can be justified by that the channel energy spreads over more multipath components under NLOS than LOS and provides richer information of the environment. Similar to the results of Exp. 1a, we find that a larger W_e mitigates the location ambiguity and enhances the overall IPS performance, with $\overline{P}_D' = 100\%$ and $\overline{P}_{\text{FA}}' = 1.65\%$ when $W_e = 321$ MHz. Additionally, from Fig. 8, we observe that $\overline{\Gamma^\star}$ decreases more rapidly when W_e enlarges than the LOS case, reducing $\overline{\Gamma^\star}$ from 0.78 under $W_e = 36$ MHz to 0.53 when $W_e = 321$ MHz.

The negligible false alarm rates in Exp. 1 also imply that the localization error is 0 cm under most cases. In fact, the false alarm rates can be further reduced by increasing $\overline{\Gamma^\star}$, leading to a false alarm rate of 0.06% and a detection rate of 99.48% under $\overline{\Gamma^\star} = 0.74$ for the LOS case, and 0% false alarm rate and a detection rate of 99.45% under $\overline{\Gamma^\star} = 0.71$.

3) Exp. 2 (Effect of Human Activities): Fig. 9 shows the impact of human activities on the performance of the proposed IPS. From Fig. 9(a)–(c), we find that a large W_e improves the robustness against environment dynamics. Fig. 9(d) illustrates the ROC curve using different W_e and further verifies that a large W_e can enhance the localization performance, leading to $\overline{P}_D' = 99.88\%$ and $\overline{P}_{\text{FA}}' = 1.66\%$ when $W_e = 321$ MHz. As shown in Fig. 8, when $W_e = 321$ MHz, a threshold of 0.52 suffices to achieve a good performance.

4) Exp. 3 (Impact of Furniture Movement): In Fig. 10, we show the performance in the presence of furniture movement. Similar to the observations in Exps. 1 and 2, a larger W_e enhances the robustness against the dynamics from furniture movement and reduces ambiguity among locations. As can be seen from Fig. 10, locations 1 and 2 are highly correlated implied by a large TRRS value, and the ambiguity between locations 1 and 2 is alleviated when W_e increases to 178 and 321 MHz, leading to an improved detection rate and false alarm rate. When $W_e = 321$ MHz, we achieve

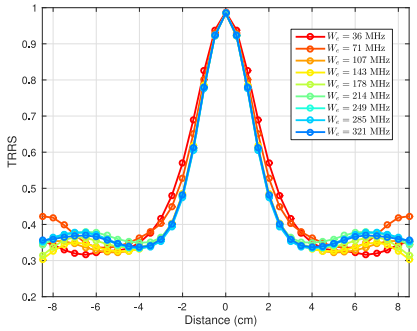

Fig. 14. Decaying of TRRS with distance in Exp. 5.

$\overline{P}_D' = 98.86\%$ and $\overline{P}_{\text{FA}}' = 1.95\%$ under a threshold of 0.50 as shown in Fig. 8.

Also, we notice that the performance does not improve monotonically with W_e. This is because the quality of different links in the multi-antenna WiFi system differs due to the discrepancy in their noise and interference levels. Thus, combining multiple links based on the channel energies might not be optimal in this case. This can be solved by calculating the TRRS using criterion robust against noise and interference on different WiFi links.

5) Exp. 4 (Impact of Door): The impact of door status on localization is more severe than the human activities when the door acts as a major reflector in the propagation of electromagnetic waves and thus its status greatly affects the CFRs.

In Fig. 11, we illustrate the results under different W_e. Obviously, a large W_e is indispensable in this case, since the TRRS values measured at locations 1 and 2 degrade to 0.42 and 0.17 under different door status with $W_e = 36$ MHz, and the IPS fails to find a $\Gamma^\star$ to achieve at least 95% detection rate and at most 2% false alarm rate. On the other hand, increasing W_e increases to 321 MHz partially recovers the similarities of the CFRs collected at the same location with different door status, and we achieve $\overline{P}_D' = 98.39\%$ and $\overline{P}_{\text{FA}}' = 1.43\%$. This could be justified by the inherent spatial diversity naturally existing in multi-antenna WiFi systems since different links can be considered uncorrelated and thus sense the environment from different perspectives. Therefore, even the door affects a majority of the multipath components on some WiFi links, its impact on other WiFi links is much less pronounced. Fig. 8 shows that the target of more than 95% detection rate and less than 2% false alarm rate is achievable when $W_e \geq 249$ MHz. In conclusion, a large W_e is paramount for the proposed IPS when there exists strong environmental dynamics.

6) Impact of Effective Bandwidth on the CDF of TRRS: We observe from the analysis on the results of Exps. 1–4 that the gap between the TRRS measured at the same locations and among different locations enlarges with respect to an increased W_e. To further validate the observation, we draw the cumulative density functions (CDFs) of the TRRS values in Fig. 12 under various W_e, where the solid lines represent the CDFs with $W_e = 321$ MHz. It shows that the TRRS values among different locations are more concentrated in a region with a small average of TRRS when W_e is large, while the

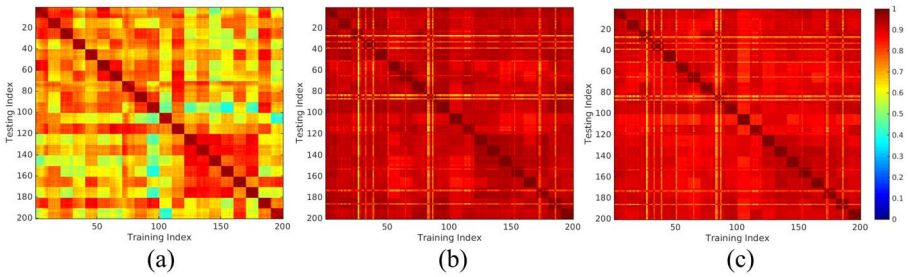

Fig. 15. Results of Exp. 6. (a) $W_e = 36$ MHz. (b) $W_e = 178$ MHz. (c) $W_e = 321$ MHz.

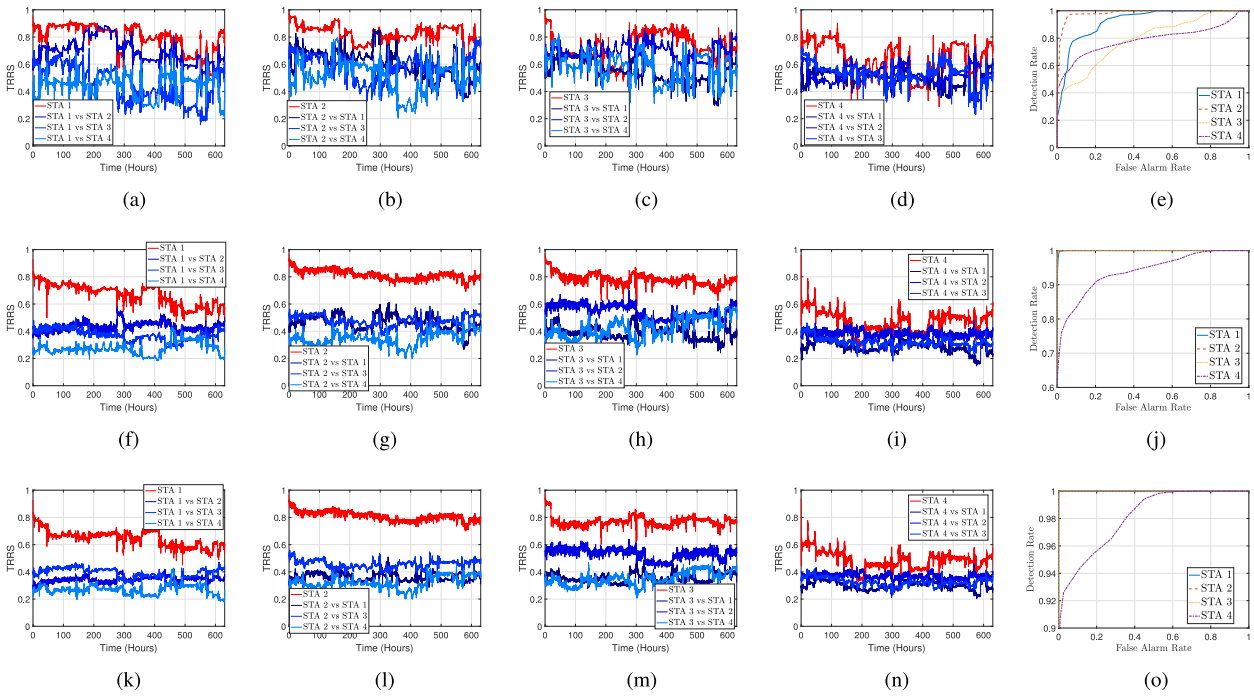

Fig. 16. Results of Exp. 7 over 26 days of measurement. (a) STA 1, $W_e = 36$ MHz. (b) STA 2, $W_e = 36$ MHz. (c) STA 3, $W_e = 36$ MHz. (d) STA 4, $W_e = 36$ MHz. (e) $W_e = 36$ MHz, ROC. (f) STA 1, $W_e = 178$ MHz. (g) STA 2, $W_e = 178$ MHz. (h) STA 3, $W_e = 178$ MHz. (i) STA 4, $W_e = 178$ MHz. (j) $W_e = 178$ MHz, ROC. (k) STA 1, $W_e = 321$ MHz. (l) STA 2, $W_e = 321$ MHz. (m) STA 3, $W_e = 321$ MHz. (n) STA 4, $W_e = 321$ MHz. (o) $W_e = 321$ MHz, ROC.

TRRS values measured at the same locations are still highly concentrated in a region with an average TRRS close to 1 for Exp. 1a and b. The decrease of the TRRS at the same location is more significant for Exps. 2–4. Yet, the degradation is still within the tolerance level as implied by the $\overline{P}_D'$ and $\overline{P}_{\text{FA}}'$ performances. Therefore, it is crucial to use a large W_e to enhance both performance and robustness.

7) Exp. 5 (Results Under 0.5 cm Measurement Resolution): Fig. 13(a)–(c) visualizes the TRRS matrix $\mathbf{R}$ calculated under different W_e. We observe that large TRRS values are highly concentrated within a small and uniform circular area with a radius of 1–2 cm surrounding the middle point when $W_e \geq 178$ MHz, while the TRRS are more decentralized when $W_e = 36$ MHz.

Fig. 14 shows the average TRRS decay along different directions calculated using $\mathbf{R}$. A larger W_e accelerates the decay of the TRRS values and improves the location distinction. With a distance larger than 1 cm, the TRRS drops below 0.75. Therefore, with an appropriate threshold, the proposed IPS can achieve an accuracy of 1–2 cm.

8) Exp. 6 (Impact of Power Cycling on Localization Performance): Fig. 15 shows $\mathbf{R}$ with different W_e for Exp. 7. Clearly, when $W_e = 36$ MHz, there exists large fluctuation in the TRRS and the localization performance is deteriorated. The performance loss can be remedied by using $W_e \geq 178$ MHz, which again demonstrates the importance of a large W_e.

9) Exp. 7 (Localization Performance Over 26 Days): In Fig. 16, we sketch the time evolution of the TRRS evaluated at the same STA locations and among different STA locations for different STAs in the 26 days of measurement. We observe that the TRRS changes with time due to the environment variations. We also find that when $W_e = 321$ MHz, the decay in TRRS is less severe than the case with $W_e = 36$ MHz.

In Fig. 16(e), (j), and (o), we display the ROC curves for the four STAs under different W_e. Obviously, in comparison with the results of $W_e = 36$ MHz, using a W_e as large as 178 and 321 MHz combats the degradation incurred by inevitable environment changes and improves the IPS performance by a large margin. Therefore, using a large W_e can greatly reduce

TABLE I
PERFORMANCES WITH $\Gamma = 0.60$ AND $W_e = 321$ MHZ

	Exp. 1 LOS	Exp. 1 NLOS	Exp. 2 Human Activities	Exp. 3 Furniture Movement	Exp. 4 Door Effect
Detection Rate (%)	99.94	100	99.72	96.61	85.00
False Alarm Rate (%)	3.96	0.14	0.01	0	0

the overhead introduced by the training phase since it becomes unnecessary to update $\mathbf{D}_{\text{train}}$ frequently.

Although the distances between the STAs in this experiment exceed 5 cm, the results would be very similar if these STAs are placed closer at a centimeter level with a large W_e. This is because the TRRS values calculated between two locations are identical as long as the distance between them exceeds 5 cm as shown in Figs. 6 and 7.

10) Results Under Universal $\Gamma^\star$: In Exps. 1–4, we assume that the proposed IPS learns a specific $\Gamma^\star$ from $\mathbf{D}_{\text{train}}$ to achieve $\overline{P}_D' \geq 95\%$ and $\overline{P}_{\text{FA}}' \leq 2\%$. In practice, due to the randomness of the environment, we might only be able to roughly find a fixed $\Gamma^\star$ based on a very limited training database without much dynamics and the performance might degrade consequently. To investigate the performance loss under a fixed $\Gamma^\star$, we configure $\Gamma^\star$ as 0.6 and W_e as 321 MHz.

The performances are summarized into Table I, which shows that except Exp. 4, the proposed IPS still achieves a detection rate higher than 96.61% with a false alarm rate smaller than 3.96%. The performance of Exp. 4 degrades but still maintains a detection rate of 85% and a false alarm rate of 0.

In practice, we perform a large number of experiments in a variety of environment. The results reveal that the 1–2 cm accuracy is universal instead of limited only to a small area, given that the number of multipath components is sufficient.

VI. CONCLUSION

In this paper, we propose a WiFi-based IPS leveraging the TR focusing effect that achieves centimeter-level accuracy for indoor localization. The proposed IPS fully utilize the spatial diversity in MIMO-OFDM WiFi systems to formulate a large effective bandwidth. Extensive experimental results show that with a measurement resolution of 5 cm, the proposed IPS achieves true positive rates of 99.91% and 100%, and incurs false positive rates of 1.81% and 1.65% under the LOS and NLOS scenarios, respectively. Meanwhile, the IPS is robust against the environment dynamics caused by human activities and object movements. Experiment results with a measurement resolution of 0.5 cm demonstrate a localization accuracy of 1–2 cm achieved by the proposed IPS.

REFERENCES

[1] T. J. Gallagher, B. Li, A. G. Dempster, and C. Rizos, "A sector-based campus-wide indoor positioning system," in *Proc. IEEE Int. Conf. Indoor Position. Indoor Navig. (IPIN)*, Zürich, Switzerland, 2010, pp. 1–8.

[2] K.-L. Sue, "MAMBO: A mobile advertisement mechanism based on obscure customer's location by RFID," in *Proc. IEEE Int. Conf. Comput. Meas. Control Sens. Netw. (CMCSN)*, Taiyuan, China, 2012, pp. 425–428.

[3] L. Wang, W. Liu, N. Jing, and X. Mao, "Simultaneous navigation and pathway mapping with participating sensing," *Wireless Netw.*, vol. 21, no. 8, pp. 2727–2745, 2015.

[4] H. Liu, H. Darabi, P. Banerjee, and J. Liu, "Survey of wireless indoor positioning techniques and systems," *IEEE Trans. Syst., Man, Cybern. C, Appl. Rev.*, vol. 37, no. 6, pp. 1067–1080, Nov. 2007.

[5] P. Bahl and V. Padmanabhan, "RADAR: An in-building RF-based user location and tracking system," in *Proc. IEEE INFOCOM*, vol. 2. Tel Aviv, Israel, 2000, pp. 775–784.

[6] M. Youssef and A. Agrawala, "The Horus WLAN location determination system," in *Proc. 3rd Int. Conf. Mobile Syst. Appl. Services (MobiSys)*, Seattle, WA, USA, 2005, pp. 205–218.

[7] P. Prasithsangaree, P. Krishnamurthy, and P. Chrysanthis, "On indoor position location with wireless LANs," in *Proc. 13th IEEE Int. Symp. Pers. Indoor Mobile Radio Commun.*, vol. 2. Lisbon, Portugal, Sep. 2002, pp. 720–724.

[8] S. Sen, B. Radunovic, R. R. Choudhury, and T. Minka, "You are facing the Mona Lisa: Spot localization using PHY layer information," in *Proc. 10th Int. Conf. Mobile Syst. Appl. Services (MobiSys)*, Ambleside, U.K., 2012, pp. 183–196.

[9] J. Xiao, K. Wu, Y. Yi, and L. M. Ni, "FIFS: Fine-grained indoor fingerprinting system," in *Proc. 21st Int. Conf. Comput. Commun. Netw. (ICCCN)*, Munich, Germany, Jul. 2012, pp. 1–7.

[10] Y. Chapre, A. Ignjatovic, A. Seneviratne, and S. Jha, "CSI-MIMO: Indoor Wi-Fi fingerprinting system," in *Proc. IEEE 39th Conf. Local Comput. Netw. (LCN)*, Edmonton, AB, Canada, Sep. 2014, pp. 202–209.

[11] Z.-H. Wu, Y. Han, Y. Chen, and K. J. R. Liu, "A time-reversal paradigm for indoor positioning system," *IEEE Trans. Veh. Technol.*, vol. 64, no. 4, pp. 1331–1339, Apr. 2015.

[12] B. Wang, Y. Wu, F. Han, Y.-H. Yang, and K. J. R. Liu, "Green wireless communications: A time-reversal paradigm," *IEEE J. Sel. Areas Commun.*, vol. 29, no. 8, pp. 1698–1710, Sep. 2011.

[13] C. Chen, Y. Chen, H.-Q. Lai, Y. Han, and K. J. R. Liu, "High accuracy indoor localization: A WiFi-based approach," in *Proc. IEEE Int. Conf. Acoust. Speech Signal Process. (ICASSP)*, Shanghai, China, Mar. 2016, pp. 6245–6249.

[14] C. Chen, Y. Chen, Y. Han, H.-Q. Lai, and K. J. R. Liu, "Achieving centimeter accuracy indoor localization on WiFi platforms: A frequency hopping approach," *IEEE Internet Things J.*, vol. 4, no. 1, pp. 111–121, Feb. 2017.

[15] J. Hightower, R. Want, and G. Borriello, "SpotON: An indoor 3D location sensing technology based on RF signal strength," Dept. Comput. Sci. Eng., Univ. Washington, Seattle, WA, USA, Tech. Rep. UW CSE 00-02-02, Feb. 2000.

[16] L. Ni, Y. Liu, Y. C. Lau, and A. P. Patil, "LANDMARC: Indoor location sensing using active RFID," in *Proc. 1st IEEE Int. Conf. Pervasive Comput. Commun. (PerCom)*, Fort Worth, TX, USA, Mar. 2003, pp. 407–415.

[17] X. Li, K. Pahlavan, M. Latva-Aho, and M. Ylianttila, "Comparison of indoor geolocation methods in DSSS and OFDM wireless LAN systems," in *Proc. IEEE-VTS Fall VTC 52nd Veh. Technol. Conf.*, vol. 6. Boston, MA, USA, 2000, pp. 3015–3020.

[18] N. S. Correal, S. Kyperountas, Q. Shi, and M. Welborn, "An UWB relative location system," in *Proc. IEEE Conf. Ultra Wideband Syst. Technol.*, Reston, VA, USA, Nov. 2003, pp. 394–397.

[19] *Ubisense.* Accessed on Apr. 13, 2016. [Online]. Available: http://ubisense.net/

[20] B. Campbell, P. Dutta, B. Kempke, Y.-S. Kuo, and P. Pannuto, "Decawave: Exploring state of the art commercial localization," Tech. Rep., Electr. Eng. Comput. Sci. Dept., Univ. Michigan, Ann Arbor, MI, USA, 2015.

[21] *Dart Ultra wideband (UWB) Technology*. Accessed on Apr. 13, 2016. [Online]. Available: https://www.zebra.com/us/en/solutions/location-solutions/enabling-technologies/dart-uwb.html

[22] J. Xiong and K. Jamieson, "Arraytrack: A fine-grained indoor location system," in *Proc. 10th USENIX Conf. Netw. Syst. Design Implement. (NSDI)*, Lombard, IL, USA, 2013, pp. 71–84.

[23] R. Schmidt, "Multiple emitter location and signal parameter estimation," *IEEE Trans. Antennas Propag.*, vol. 34, no. 3, pp. 276–280, Mar. 1986.

[24] J. Gjengset, J. Xiong, G. McPhillips, and K. Jamieson, "Phaser: Enabling phased array signal processing on commodity WiFi access points," in *Proc. 20th Annu. Int. Conf. Mobile Comput. Netw. (MobiCom)*, Maui, HI, USA, 2014, pp. 153–164.

[25] M. Kotaru, K. Joshi, D. Bharadia, and S. Katti, "SpotFi: Decimeter level localization using WiFi," *SIGCOMM Comput. Commun. Rev.*, vol. 45, no. 4, pp. 269–282, Aug. 2015.
[26] B. Bogert, "Demonstration of delay distortion correction by time-reversal techniques," *IRE Trans. Commun. Syst.*, vol. 5, no. 3, pp. 2–7, Dec. 1957.
[27] J. Kormylo and V. Jain, "Two-pass recursive digital filter with zero phase shift," *IEEE Trans. Acoust. Speech Signal Process.*, vol. 22, no. 5, pp. 384–387, Oct. 1974.
[28] M. Fink, "Acoustic time-reversal mirrors," in *Imaging of Complex Media With Acoustic and Seismic Waves* (Topics in Applied Physics), vol. 84, M. Fink, W. A. Kuperman, J.-P. Montagner, and A. Tourin, Eds. Heidelberg, Germany: Springer, 2002.
[29] M. Fink, C. Prada, F. Wu, and D. Cassereau, "Self focusing in inhomogeneous media with time reversal acoustic mirrors," in *Proc. IEEE Ultrason. Symp.*, vol. 2. Montreal, QC, Canada, Oct. 1989, pp. 681–686.
[30] C. Dorme, M. Fink, and C. Prada, "Focusing in transmit-receive mode through inhomogeneous media: The matched filter approach," in *Proc. IEEE Ultrason. Symp.*, vol. 1. Tucson, AZ, USA, Oct. 1992, pp. 629–634.
[31] F. Han, Y.-H. Yang, B. Wang, Y. Wu, and K. J. R. Liu, "Time-reversal division multiple access over multi-path channels," *IEEE Trans. Commun.*, vol. 60, no. 7, pp. 1953–1965, Jul. 2012.
[32] G. L. Stuber *et al.*, "Broadband MIMO-OFDM wireless communications," *Proc. IEEE*, vol. 92, no. 2, pp. 271–294, Feb. 2004.
[33] M. Speth, S. A. Fechtel, G. Fock, and H. Meyr, "Optimum receiver design for wireless broad-band systems using OFDM—Part I," *IEEE Trans. Commun.*, vol. 47, no. 11, pp. 1668–1677, Nov. 1999.

Chen Chen (S'15) received the B.S. and M.S. degrees from the Department of Microelectronics, Fudan University, Shanghai, China, in 2010 and 2013, respectively. He is currently pursuing the Ph.D. degree at the Department of Electrical and Computer Engineering, University of Maryland at College Park, College Park, MD, USA.

His research interests include biomedical signal processing, indoor localization, and wireless communications.

Mr. Chen was the recipient of multiple honors and awards, including the Best Student Paper Award of the IEEE ICASSP 2016, the Litton Industries Fellowship from the University of Maryland at College Park in 2015, the Distinguished Graduate Student Teaching Award from the University of Maryland at College Park in 2014, and the Excellent Graduate Student of Shanghai in 2013.

Yan Chen (SM'14) received the bachelor's degree from the University of Science and Technology of China, Hefei, China, in 2004, the M.Phil. degree from the Hong Kong University of Science and Technology, Hong Kong, in 2007, and the Ph.D. degree from the University of Maryland at College Park, College Park, MD, USA, in 2011.

Being a founding member, he joined Origin Wireless Inc., Greenbelt, MD, USA, as a Principal Technologist in 2013. He is currently a Professor with the University of Electronic Science and Technology of China, Chengdu, China. His research interests include multimedia, signal processing, game theory, and wireless communications.

Dr. Chen was the recipient of multiple honors and awards, including the Best Student Paper Award of IEEE ICASSP in 2016, the Best Paper Award of IEEE GLOBECOM in 2013, the Future Faculty Fellowship and Distinguished Dissertation Fellowship Honorable Mention from the Department of Electrical and Computer Engineering in 2010 and 2011, the Finalist of the Dean's Doctoral Research Award from the A. James Clark School of Engineering, University of Maryland at College Park in 2011, and the Chinese Government Award for outstanding students abroad in 2010.

Yi Han (GS'14–M'15) received the B.S. degree in electrical engineering (with highest honor) from Zhejiang University, Hangzhou, China, in 2011, and the Ph.D. degree from the Department of Electrical and Computer Engineering, University of Maryland at College Park, College Park, MD, USA.

He is currently the Wireless Architect with Origin Wireless Inc., Greenbelt, MD, USA. His research interests include wireless communication and signal processing.

Dr. Han was the recipient of Best Student Paper Award of IEEE ICASSP in 2016 and the Class A Scholarship from Chu Kochen Honors College, Zhejiang University in 2008.

Hung-Quoc (Quoc) Lai (M'11) received the B.S. *(cum laude)*, M.S., and Ph.D. degrees in electrical engineering from the University of Maryland at College Park, College Park, MD, USA, in 2004, 2006, and 2011, respectively.

He is a founding member and currently the Vice President of Engineering with Origin Wireless Inc., Greenbelt, MD, USA, which develops advanced time reversal wireless technologies for use in a wide variety of applications of indoor positioning/tracking, monitoring, security, radio human biometrics, wireless power transfer, and 5G communications. Prior to joining Origin Wireless Inc. in 2013, he was a Technical Lead in research and development of multiple-input multiple-output (MIMO) and cooperative communications with the U.S. Army RDECOM CERDEC, Aberdeen Proving Ground, MD, USA. He is a Gates Millennium Scholar.

Feng Zhang (S'11) received the B.S. and M.S. degrees from the Department of Electronic Engineering and Information Science, University of Science and Technology of China, Hefei, China, in 2011 and 2014, respectively. He is currently pursuing the Ph.D. degree at the Department of Electrical and Computer Engineering, University of Maryland at College Park, College Park, MD, USA.

His research interests include time reversal communications, wireless signal processing, and indoor localization.

Mr. Zhang was a recipient of the Distinguished Graduate Student Teaching Award of the University of Maryland at College Park in 2015 and the China National Scholarship in 2014.

K. J. Ray Liu (F'03) was named a Distinguished Scholar–Teacher of the University of Maryland at College Park, College Park, MD, USA, in 2007, where he is Christine Kim Eminent Professor of Information Technology. He leads the Maryland Signals and Information Group, conducting research encompassing broad areas of information and communications technology with a recent focus on smart radios for smart life.

Dr. Liu was a recipient of the 2016 IEEE Leon K. Kirchmayer Technical Field Award on graduate teaching and mentoring, the IEEE Signal Processing Society 2014 Society Award, and the IEEE Signal Processing Society 2009 Technical Achievement Award. He was also the recipient of teaching and research recognitions from the University of Maryland at College Park, including the university-level Invention of the Year Award and college-level Poole and Kent Senior Faculty Teaching Award, Outstanding Faculty Research Award, and Outstanding Faculty Service Award, all from the A. James Clark School of Engineering. Recognized by Thomson Reuters as a Highly Cited Researcher. He is a Fellow of the AAAS. He is a member of the IEEE Board of Director. He was President of the IEEE Signal Processing Society, where he has served as Vice President–Publications and Board of Governor. He has also served as the Editor-in- Chief of *IEEE Signal Processing Magazine*.